LAWRENCE
LIVERMORE
NATIONAL
LABORATORY

Optical and X-ray Characterization of Groove Profiles in DT Ice Layers

J. A. Koch, B. J. Kozioziemski, J. Salmonson, A. Chernov, L. J. Atherton, E. Dewald, N. Izumi, M. A. Johnson, S. Kucheyev, J. Lugten, E. Mapoles, J. D. Moody, J. W. Pipes, J. D. Sater, D. Stefanescu

July 8, 2008

18th Target Fabrication Meeting
Lake Tahoe, CA, United States
May 11, 2008 through May 15, 2008

Disclaimer

This document was prepared as an account of work sponsored by an agency of the United States government. Neither the United States government nor Lawrence Livermore National Security, LLC, nor any of their employees makes any warranty, expressed or implied, or assumes any legal liability or responsibility for the accuracy, completeness, or usefulness of any information, apparatus, product, or process disclosed, or represents that its use would not infringe privately owned rights. Reference herein to any specific commercial product, process, or service by trade name, trademark, manufacturer, or otherwise does not necessarily constitute or imply its endorsement, recommendation, or favoring by the United States government or Lawrence Livermore National Security, LLC. The views and opinions of authors expressed herein do not necessarily state or reflect those of the United States government or Lawrence Livermore National Security, LLC, and shall not be used for advertising or product endorsement purposes.

Optical and X-ray Characterization of Groove Profiles
in DT Ice Layers

J. A. Koch, B. J. Kozioziemski, J. Salmonson, A. Chernov, L. J. Atherton,

E. Dewald, N. Izumi, M. A. Johnson, S. Kucheyev, J. Lugten, E. Mapoles,

J. D. Moody, J. W. Pipes, J. D. Sater, D. Stefanescu

Lawrence Livermore National Laboratory

P.O. Box 808, L-481, Livermore CA

Abstract

Deuterium-tritium (DT) single-crystal ice layers in spherical shells often form with localized defects that we believe are vapor-etched grain boundary grooves built from dislocations and accommodating slight misorientations between contacting lattice regions. Ignition implosion target requirements limit the cross-sectional areas and total lengths of these grooves, and since they are often the dominant factor in determining layer surface quality, it is important that we be able to characterize their depths, widths and lengths. We present a variety of raytracing and diffraction image modeling results that support our understanding of the profiles of the grooves, which is grounded in x-ray and optical imaging data, and we describe why these data are nevertheless insufficient to adequately determine whether or not a particular layer will meet the groove requirements for ignition. We present accumulated data showing the distribution of groove depths, widths, and lengths from a number of layers, and we discuss how these data motivate the adoption of layer rejection criteria in order to ensure that layers that pass these criteria will almost certainly meet the groove requirements.

I. Introduction

Our understanding of the structure of deuterium-tritium (DT) ice layers in spherical shells has been greatly advanced by the accumulation of optical imaging data supporting the hypothesis that the best (smoothest) layers form as a single HCP crystal from a small seed having it's c-axis oriented along the shell surface [1]. We now interpret structure observed during layer formation (Fig. 1) in these terms, and we believe that most imperfections in the layers are caused by deviations from perfect single-crystal structure. The most important defects we observe in layers are long linear features (Fig. 2). These features are now understood to be low-angle grain boundary grooves on the inner ice surface, separating regions of DT ice having slightly different crystal orientations. These grooves have some distribution of lengths, depths, and width, as discussed below.
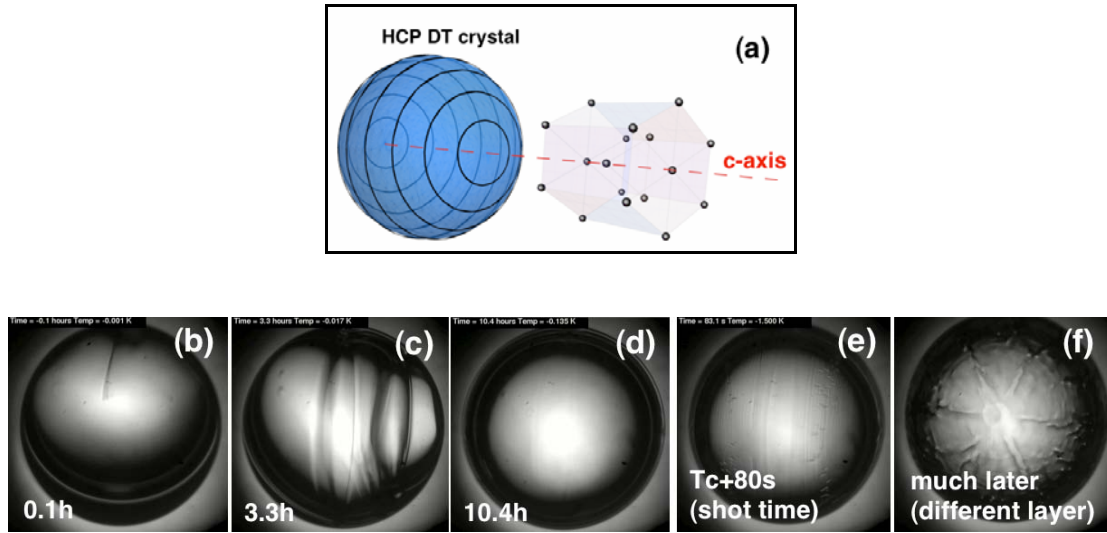

Figure 1: (a) Globe symmetry of DT layers results from HCP single crystal symmetry with a c-axis in a specific direction. (b)-(f) Sequence of optical images of a DT layer taken at different times, (b) t=0.1 hours after cooling below the triple point, a long crystal begins to wrap around the shell, (c) t=3.3 hours, band has formed a ring that grows slowly towards two poles, (d) t=10.4 hours, single crystal layer is complete, (e) 80 seconds after rapidly cooling to 1.5 degrees below the DT triple point, a series of ripples appear along lines of latitude, (f) a different rapidly cooled layer viewed along the c-axis long after rapid cooling is complete, showing 6-fold symmetry indicative of underlying HCP crystal symmetry.
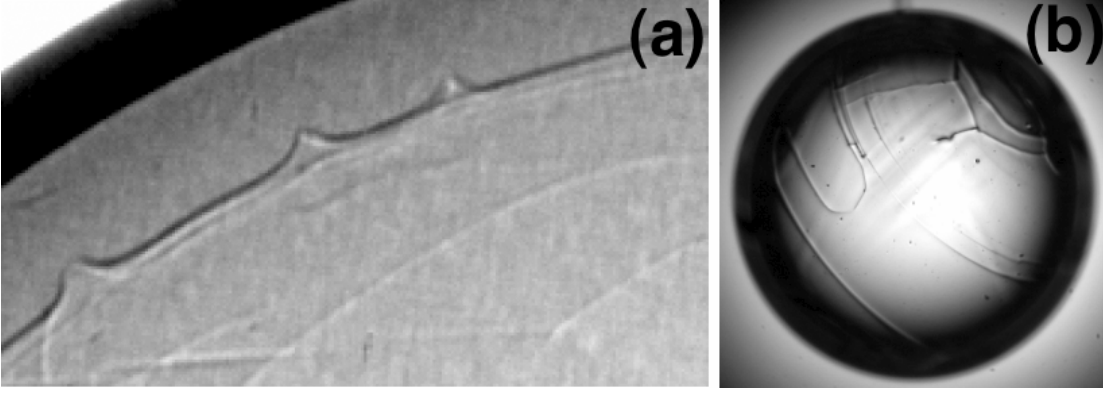
Figure 2: Grain boundary grooves in the inner surface of DT layers, (a) viewed nearly edge-on with x-ray radiography, (b) viewed with backlit optical imaging.

From theoretical considerations [1], we expect the groove profiles to follow a cusp shape with an equation of the form,

$$y = \frac{A}{\left(1 + \frac{|x|}{w}\right)^2} \tag{1}$$

where y is the depth of the groove at a distance x from the central peak, A is the maximum depth at x = 0, and w is the half-width at 1/4 maximum depth. The parameters A and w depend on the interfacial crystal/vapor and grain boundary energies, the ice temperature, the β-decay heat generation rate, the ice thermal conductivity, and the ice sublimation heat. Generally, we cannot predict the grain boundary energy for any particular groove in any particular layer, so we need to rely on experimental measurements of both A and w.

Ignition experiments at the National Ignition Facility (NIF) place stringent requirements on the smoothness of the inner ice surface, with specific requirements on the maximum high-mode surface roughness as measured along the limb, maximum mode-by-mode deviations from sphericity for low-mode perturbations measured along the limb, and maximum groove K parameter [2],

$$K \equiv \sqrt{\frac{1}{V_{\text{fuel}}} \sum_{j=1}^{\text{all grooves}} A_j^2 w_j^2 L_j} \; < \; 0.7 \; \mu m \tag{2}$$

where V_{fuel} is the total volume of DT ice, and A_j, w_j, and L_j are the depth, width and length of groove j. We have developed reliable techniques to measure high- and low-mode surface perturbations along the limb [3, 4, 5], but we do not currently have the ability to accurately quantify K for any particular layer.

In this paper we describe the techniques we use to characterize grooves in DT ice layers, and we discuss advantages, disadvantages and limitations for both optical imaging (for optically transparent shells) and x-ray imaging (for optically transparent and opaque shells) based on experiments and simulations. We also present a statistical approach to estimating probability distributions for the groove depth, width, and length, and therefore the probability distribution for K. This approach allows us to develop pass/fail criteria based directly on measurements we can make, and we conclude that in most cases we expect to be able to identify layers that meet the K requirement even though we cannot accurately measure K directly.

II. X-ray Imaging Diagnostics of Grooves

We use refraction-enhanced (phase contrast) x-ray imaging to characterize ice layers in both optically-opaque and optically-transparent shells [4, 5]. The diagnostic system is shown in Fig. 3 along with typical x-ray images showing the limb as well as various grooves near the limb. Absorption of 8.4 keV x-rays by the DT ice is negligible, so all contrast in the images is due to phase shifts along different paths between the source and the detector, and this can be understood as being caused by small refractive deflections of these ray paths.

When a groove cuts across the limb, we can measure it's depth directly, and if it is viewed nearly edge-on (as in Fig. 2) we can measure it's width directly. In other

cases, where the groove depths and widths aren't measurable directly, we can simulate the radiograph image for an assumed depth and width. Fig. 4 shows a
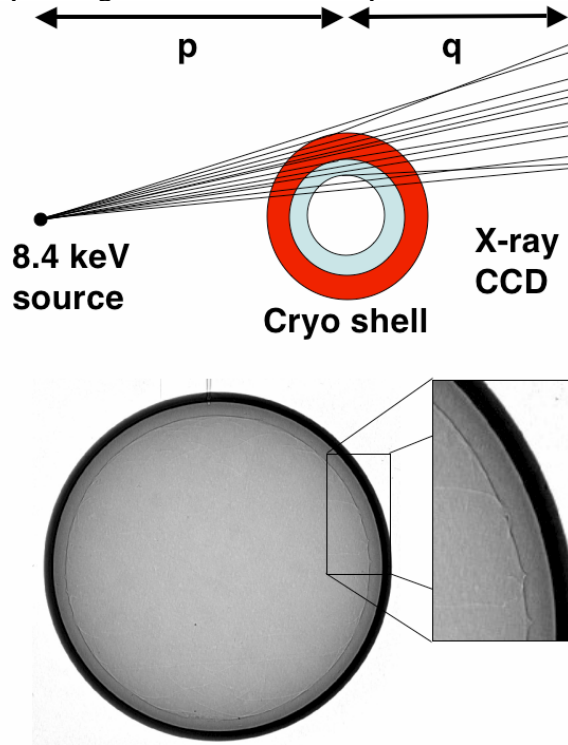

Figure 3: Schematic of x-ray imaging system, with a typical representative radiograph and a magnified region showing grooves. The source distance p is typically 75 mm, the detector distance q is typically 700 mm, and the source is typically 4 µm diameter and primarily emits W L-shell line emission near 8.4 keV.
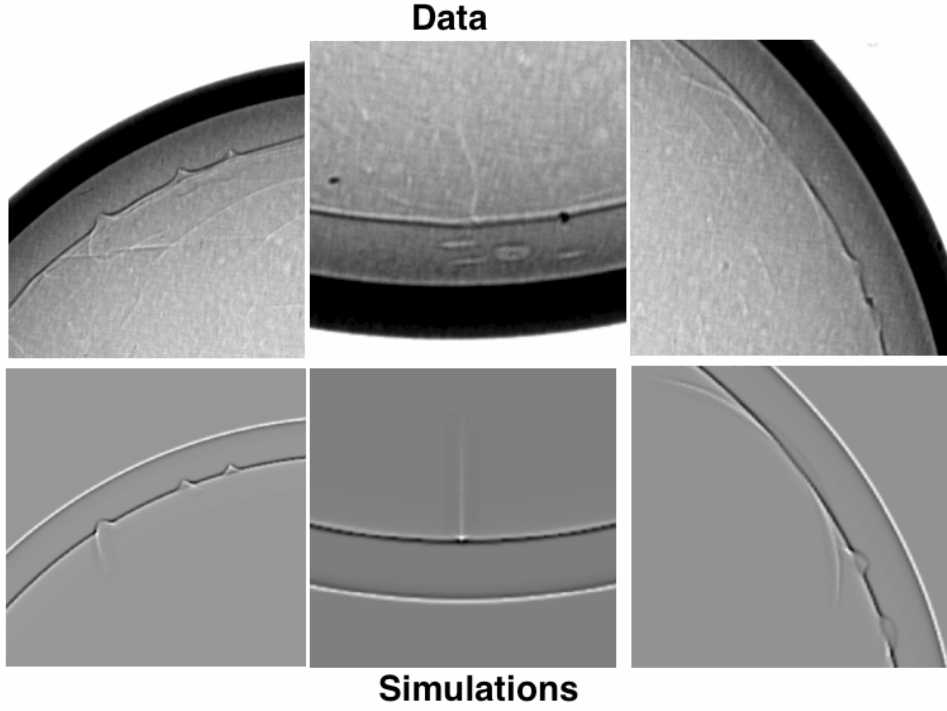
Figure 4: Groove images from three layers (top row), and corresponding simulated radiographs for the same cases (bottom row).

comparison between experimental data and simulated data for grooves with fixed depth (15 µm) and width (20 µm half-width) but with various orientations with respect to the viewing line of sight. These simulations were single-slice diffraction calculations, similar to those described in Ref. [6]. In all cases the agreement is very good, supporting the validity of eq. (1) and showing that grooves in this particular layer tend to have 15 µm depths and 20 µm half-widths. We note that grooves show reduced contrast if they are viewed more nearly face-on, and in fact with our x-ray radiography system we rarely see grooves except near the limb. Grooves that show significant contrast near the limb become invisible in the central regions of the images.

Near the central regions of the images, we can use a small-angles approximation to the geometrical optics solution for groove contrast, with the resulting predicted contrast being,

$$C = \frac{I_{peak} - I_{background}}{I_{peak} + I_{background}} = \frac{12A(\Delta n)}{\left(\dfrac{1}{p} + \dfrac{1}{q}\right)w^2} \tag{3}$$

where A and w are the amplitude and width in equation (1), p is the source/object distance, q is the detector/object distance, and Δn is the difference in the refractive index between the ice and the DT vapor at the x-ray energy being used. For our current system operating at 8.4 keV, the grooves evident near the limb in Fig. 4 would produce the noise floor contrast of 2% in the central region of the image, consistent with the fact that we don't see grooves near the central regions of these images. Fig. 5 presents single-slice diffraction calculations for various face-on groove profiles, all with constant area but with different depths and widths and very different contrast. This shows that image contrast is not simply related to depth, width, or area, but instead to cusp sharpness.
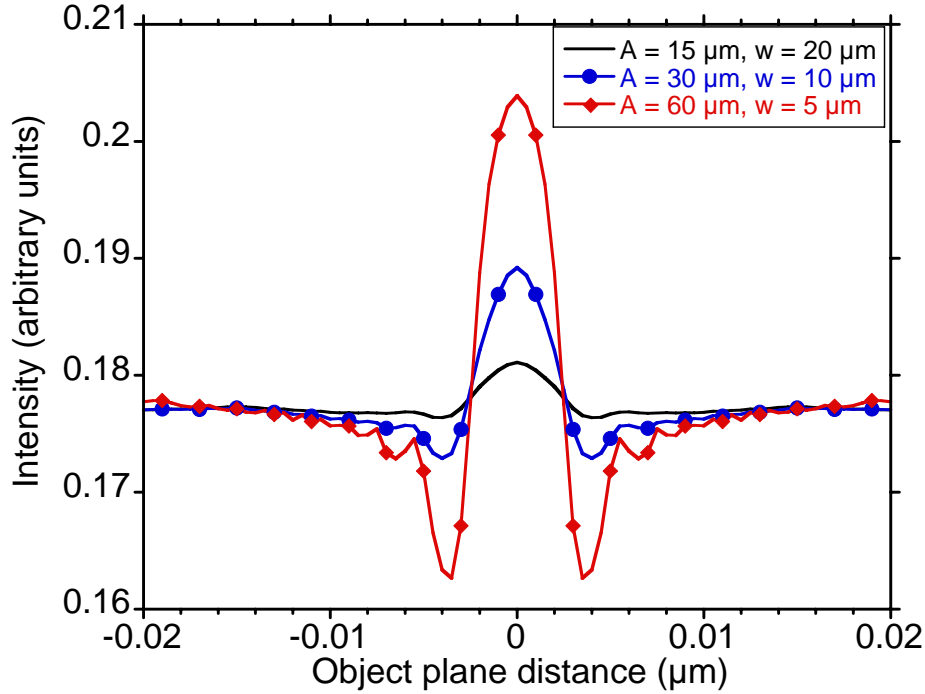

Figure 5: Simulated x-ray image profiles of various face-on grooves in an ice layer 72 µm thick backed by a plastic substrate 150 µm thick, assuming an 8.4 keV x-ray source 4 µm in diameter. Deeper and narrower grooves provide more image contrast.

In summary, x-ray radiography can provide quantitative depth information for grooves crossing the limb if the depths are not significantly smaller than our spatial resolution of 4 µm. X-ray radiography can also provide quantitative width information for those (rare) grooves that cross the limb nearly edge-on. However, for grooves that do not cross the limb, the observed contrast is a function of both depth and width as well as the position of the groove on the surface, and most grooves become invisible near the central regions of the images. It is clear that x-ray radiography alone cannot provide quantitative measurements of K for any particular layer, because we cannot detect most grooves and because we often cannot quantify groove depths and widths for the grooves we can detect.

III. Optical Imaging Diagnostics of Grooves

For ice layers in transparent shells, additional diagnostic information can be obtained from backlit optical imaging. The geometry of the system is shown in Fig. 6,
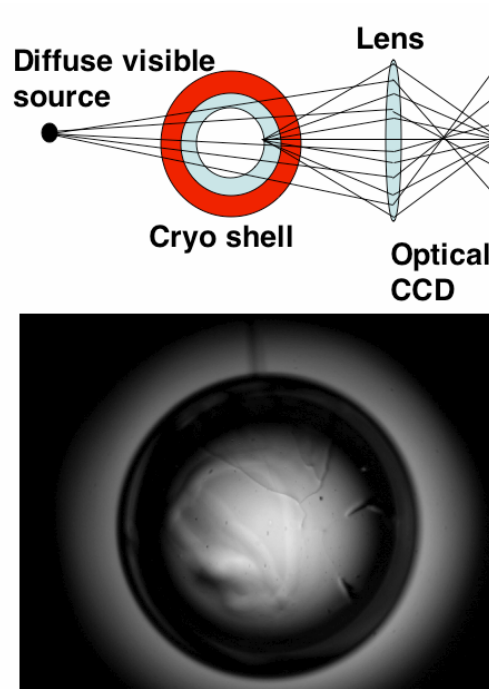
Figure 6: Schematic of optical system, with a typical representative image. The backlight source typically subtends up to f/4, and the imaging lens is typically f/4, but there are various configurations. The sharp lines in the image are grooves on the near side of the ice surface, the defocused lines are grooves in the out-of-focus far side of the ice surface.

along with a typical image showing grooves in an ice layer. From a geometrical optics perspective, refraction of light by the grooves changes the direction of rays coming from the backlight, and the imaging lens maps these deviations into apparent surpluses and deficits of observed signal.

Fig. 7(a) shows simulated raytrace images of grooves in the central region of the image, for various groove parameters A and w, and Figs. 7(b) and 7(c) show how the image profile of a particular groove varies depending on the effective numerical aperture and the focus position, respectively. We find that in general, optical imaging is much more sensitive to the presence of grooves, but cannot easily quantify the groove widths or depths because the image contrast is related to a combination of depth and width (as in eq. (3)) and varies significantly depending on
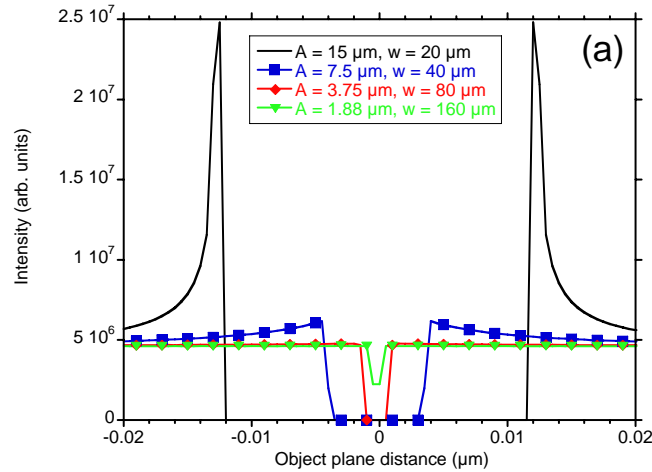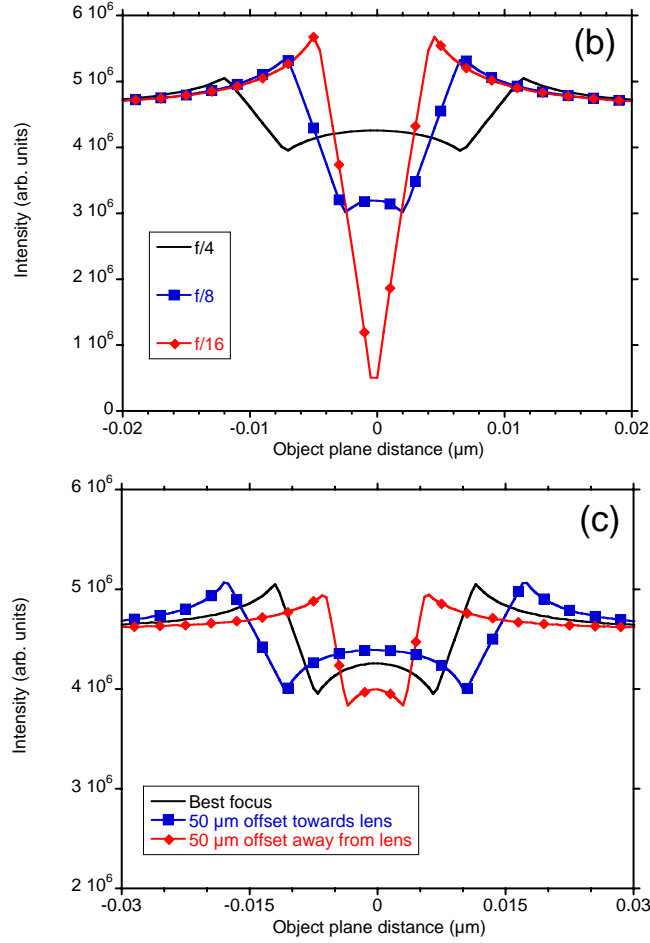
Figure 7: Intensity profiles of cusp optical images; (a) for various depths and widths at best focus and with a collimated backlight; (b) for a 2 µm deep, 20 µm wide groove at best focus, for various source numerical apertures; (c) for a 2 µm deep, 20 µm wide groove with an f/4 backlight, at various focal positions relative to the ice surface.

the details of the imaging geometry. Optical imaging is valuable for understanding the layer structure (Fig. 1) and detecting the presence of grooves, but cannot provide enough information to measure the K parameter for any particular layer.

We are therefore faced with a layer quality requirement (eq. (2)) that cannot currently be directly measured. In the following sections we develop a statistical approach to the problem that allows us to relate alternative pass/fail criteria to the groove K parameter based on measurements from a large number of layers, with the goal of identifying criteria that are essentially equivalent to meeting the K requirement.

IV. Statistical Distributions of Groove Depths, Widths and Lengths

As described in Section III, if a groove crosses the limb nearly edge-on, we can measure it's depth and width direction with x-ray radiography. In all other cases, observed image contrast is due essentially to cusp sharpness as well as experimental conditions. We will therefore explore those groove profiles we have been able to measure, and attempt to build statistical probability distributions for a groove to have a particular depth and width based on these data. We will use optical imaging data to build a similar distribution of total groove length, and we will use the depth, width and length distributions together to build a probability distribution for K. We can then apply rejection criteria to the layers, and evaluate how these criteria change the distribution function for K among those layers that pass the criteria. We note that we are particularly interested in layers that are just below the DT triple point temperature, since our current strategy for NIF targets is to form layers at this temperature and then rapidly cool them an additional 1.5K just prior to a NIF target experiment [7].

Fig. 8 shows a compilation of data points for those grooves we have been able to measure with x-ray radiography, for various layers 0.2K below the DT triple
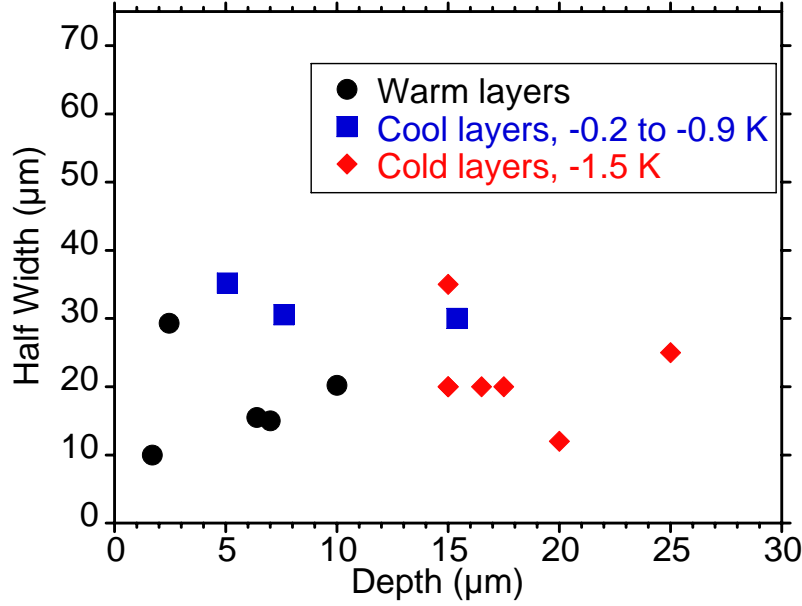
Figure 8: Compilation of groove data derived from x-ray radiography. Widths average 22 µm (half width at 1/4 maximum depth) essentially independent of layer temperature, but depths increase as the layer temperature decreases farther below the DT triple-point temperature.

point ("warm"), 1.5K below the DT triple point ("cold"), and in-between ("cool"). We see that in general, the groove widths appear to be independent of layer temperature and average 22 µm half-width. For our purposes, we assume that the groove width probability distribution is given by a Gaussian fit to all the data points (warm, cool and cold) in Fig. 8, with a center of 22.4 µm and a standard deviation (7.7 µm) given by the width of the Gaussian fit.

The groove depths in Fig. 8 scale inversely with layer temperature and are shallowest in the warm layers, which are the least plastically deformed and which are expected to have the smallest dislocation density; this in turn would give rise to the lowest lattice misorientations between grains and thus the lowest corresponding grain boundary energies. This presents a challenge, since we are most interested in warm layers and since our ability to detect and quantify shallow grooves with x-ray radiography is limited to grooves more than approximately 2 µm deep. We therefore make three different assumptions about the depth distribution function, differing in the fraction of grooves < 2 µm deep, in order to account for the fact that we cannot

measure the full distribution directly with x-ray radiography; we can only measure the distribution of grooves > 2 µm deep. The first (Depth1) is a Gaussian fit to the warm data points in Fig. 8 (mean 5.9 µm, $\sigma = 3.2$ µm, 10% of grooves < 2 µm deep), the second (Depth2) is an exponential with a mean equal to the 5.9 µm mean of the warm data points in Fig. 8 (29% of grooves < 2 µm deep), and the third (Depth3) is an exponential with a mean 1σ less than the 5.9 µm mean of the warm data points in Fig. 8 (52% of grooves < 2 µm deep).

For groove lengths, we rely on optical images, which clearly show grooves of essentially all relevant depths and widths. Fig. 9 shows a variety of optical images of warm layers, ranging from featurelessly smooth to heavily grooved. Our strategy will be to measure the total length of all grooves in the near surface (1/4 of the total surface area), separately keeping track of high-contrast grooves, low-contrast grooves (estimated from raytracing to be < 2 µm deep), and circular features often observed near the poles of the globe symmetry (contrast suggests these are also < 2 µm deep). We will then make two assumptions about how the grooves are distributed in the rest of the surface.
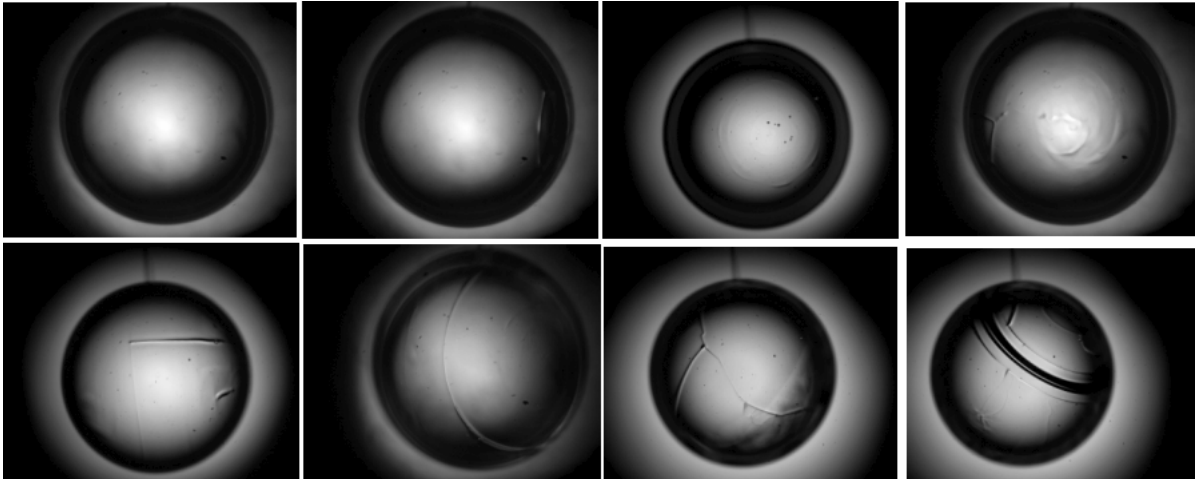

Figure 9: Optical images showing grooves in a variety of layers, ranging from featurelessly smooth to heavily grooved. All layers are "warm", at temperatures 0.2K below the DT triple point.
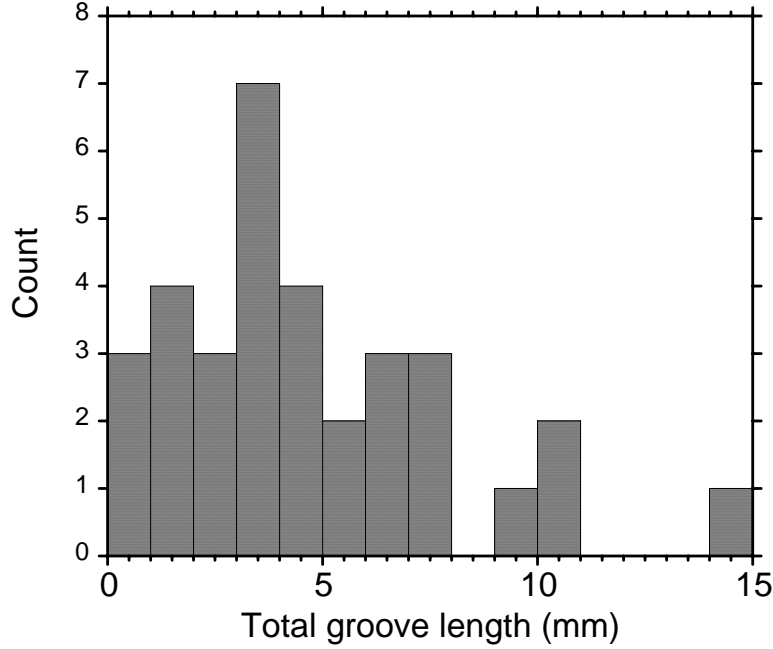
Figure 10: Histogram of total groove length derived from measuring lengths in optical images of 33 warm layers, in the area of the layer that is visible and in-focus (approximately 1/4 of the total surface area).

Fig. 10 shows the resulting near-surface length probability distribution function obtained from a collection of 33 layer images similar to those shown in Fig. 9. Approximately 25% of the total lengths are from low-contrast < 2 µm grooves, suggesting that the three depth distributions assumed above (with 10%, 29% and 52% of grooves having depths < 2 µm) probably bound the actual depth distribution function. We do not, however, know how this distribution applies to the rest of the surface that we cannot see or is out of focus; quality in one section of the surface is probably strongly but imperfectly correlated with quality in another section of the surface. We therefore assume a +/- 1 groove variation in the other 3 quarter-sections of the surface, with a length given by the mean groove length in the near surface quarter-section, and we assume a +/- 1 polar circle variation at the opposite pole (these features only occur near the poles that define the c-axis of the crystal). Finally, when the near surface does not show any of a particular class of groove (high-contrast linear, low-contrast linear, polar circle), we make two different assumptions: we assume the other quarter-sections of the surface also have none (Length1), or we add

either 0 or 1 features randomly, with a length corresponding to the average length for that type of feature (0.62 mm for high-contrast grooves, 1.07 mm for low-contrast grooves, and 2.05 mm for polar circles).

If we assume that groove depths, widths and lengths are uncorrelated and representative of what we would expect from independent layering attempts (this is an assumption), we can combine the various distributions by generating random numbers for depths, widths and lengths according to the respective distribution functions, calculating K for each set of random number sets, and then calculating the K distribution function from the entire collection of random number sets. Fig. 11 shows the resulting cumulative K distribution function for the various assumed depth and length distributions. It is clear that uncertainty in the depth distribution function is more important than uncertainty in the length distribution function, and that based on this analysis we would expect a randomly-formed layer to meet the 0.7 µm K requirement approximately 25 - 75% of the time.
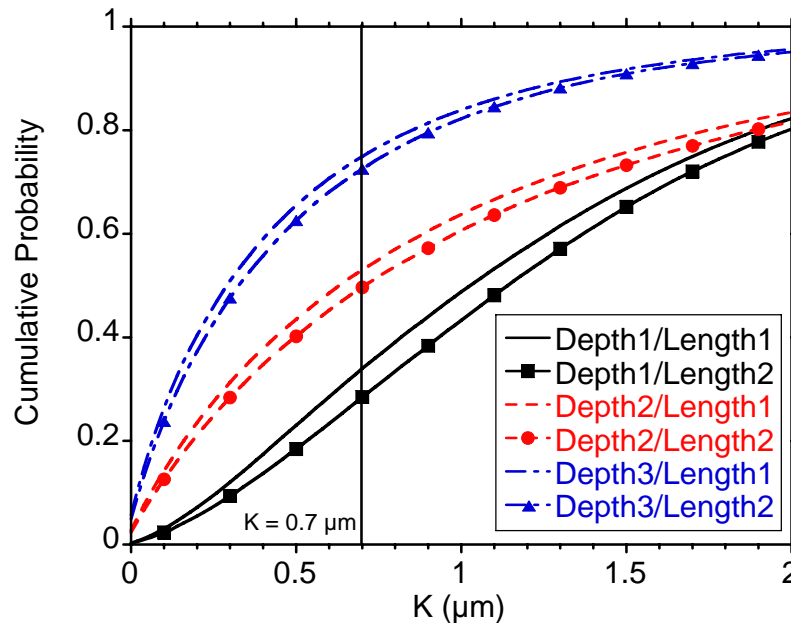

Figure 11: Cumulative K probability distribution function for the various assumed depth and length probability distribution functions, all having the same width probability distribution function.

We can then apply rejection criteria to the problem and see how the K probability distribution changes among the layers that pass the criteria. We do this by examining x-ray images that were taken for all 33 layers that comprise the length distribution data set, and eliminating those layers that do not pass two criteria: (1) No visible grooves anywhere in the x-ray images, and (2) limb power spectrum RMS (modes > 7) < 0.4 µm. We then recalculate the length probability and K-parameter distribution functions from the reduced optical image data set, which includes only layers that passed the two criteria. Fig. 12 shows the resulting cumulative K distribution function for the various assumed depth and length distributions, for those layers that meet the x-ray image criteria. We find that the above x-ray image criteria would be expected to identify most layers that fail to meet the K parameter requirement, and only 10 - 35% of layers that meet the criteria would fail to meet the requirement.
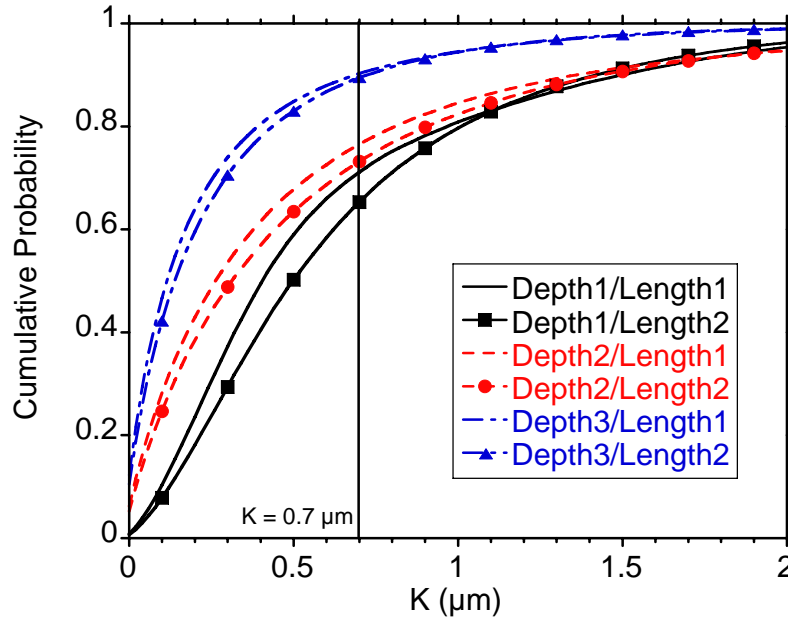

Figure 12: Cumulative K probability distribution function for the various assumed depth and length probability distribution functions, all having the same width probability distribution function, after rejecting those layers with > 0.4 µm RMS in the limb power spectrum (modes 7 and higher) or which have visible grooves in x-ray images.

V. Summary

We have shown that the dominant imperfections in DT layer surfaces are cusp-like grooves we believe to be low-angle grain boundary grooves. Ignition-quality layers must meet specific requirements on the groove K parameter, which is related to groove depths, widths, and total lengths. We can use x-ray radiography to detect many grooves, and we can quantify groove depths and sometimes widths for those grooves that appear to cross the limb of the x-ray image, but x-ray radiography fails to detect most grooves that do not appear near the limb and cannot separately quantify depths and widths for grooves that do not cross the limb. Optical imaging is very sensitive to all grooves, but can only provide combined depth and width information for shallow grooves that do not produce saturated image contrast. We therefore do not currently have an approach to quantify K for any particular layer.

We have described our statistical approach to this problem, which utilizes statistical arguments based on separate measurements of groove depths and widths from x-ray radiography, and on measurements of total groove lengths from optical imaging. This approach requires some assumptions to be made, and we use several different assumptions in the hopes of bounding the problem. We find that most warm layers are unlikely to meet the K requirement, but that if we select only layers that have (1) No visible grooves anywhere in the x-ray images, and (2) limb power spectrum RMS (modes > 7) < 0.4 µm., then those layers very probably do meet the K requirement.

In order to be more quantitative, we need improved diagnostic techniques. Increasing the wavelength λ of the x-ray backlighter will improve the visibility of shallow grooves, since Δn in eq. (3) scales as λ^2; this would allow us to detect more grooves, and could lead to the development of object phase retrieval techniques based on diffraction [7, 8]. Better modeling and a better understanding of the experimental setup may allow us to separate depth and width effects on groove contrast profiles in

optical images (Fig. 7). Finally, optical interferometry can be used to provide quantitative information about the ice surface over a large angular region.

References

[1] A. Chernov *et al.*, submitted for publication.

[2] Steve Haan, LLNL, personal communication.

[3] J. A. Koch, J. D. Sater, A. J. MacKinnon, T. P. Bernat, D. N. Bittner, G. W. Collins, B. A. Hammel, E. R. Mapoles, C. H. Still, "Numerical raytrace verification of optical diagnostics of ice surface roughness for inertial confinement fusion experiments", Fusion Science and Technology **43**, 55 (2003).

[4] B. J. Kozioziemski, J. A. Koch, A. Barty, H. E. Martz, Jr., W-K. Lee, K. Fezzaa, "Quantitative characterization of inertial confinement fusion capsules using phase contrast enhanced x-ray imaging", J. Appl. Phys. **97**, 063103 (2005).

[5] D. S. Montgomery, A. Nobile, P. J. Walsh, "Characterization of National Ignition Facility cryogenic beryllium capsules using x-ray phase contrast imaging", Rev. Sci. Instrum. **75**, 3986 (2004).

[6] H. E. Martz, Jr., B. J. Kozioziemski, S. K. Lehman, S. Hau-Riege, D. J. Schneberk, A. Barty, "Validation of radiographic simulation codes including x-ray phase effects for millimeter-size objects with micrometer structures", J. Opt. Soc. Am. A **24**, 169 (2007).

[7] J. M. Rodenburg, A. C. Hurst, A. G. Cullis, "Transmission microscopy without lenses for objects of unlimited size", Ultramicroscopy **107**, 227 (2007).

[8] J. M. Rodenburg, A. C. Hurst, A. G. Cullis, B. R. Dobson, F. Pfeiffer, O. Bunk, C. David, K. Jefimovs, I. Johnson, "Hard-x-ray lensless imaging of extended objects", Phys. Rev. Lett. **98**, 034801 (2007).